

Chemical and electronic structure analysis of a SrTiO₃ (001)/*p*-Ge (001) hydrogen evolution photocathode

Kelsey A. Stoerzinger and **Yingge Du**, Physical and Computational Sciences Directorate, Pacific Northwest National Laboratory, 902 Battelle Blvd, Richland WA 99352, USA

Steven R. Spurgeon, Energy and Environment Directorate, Pacific Northwest National Laboratory, 902 Battelle Blvd, Richland WA 99352, USA

Le Wang, Physical and Computational Sciences Directorate, Pacific Northwest National Laboratory, 902 Battelle Blvd, Richland WA 99352, USA

Demie Kepaptsoglou, SuperSTEM, SciTech Daresbury Campus, Daresbury, WA44AD, UK; Jeol Nanocentre, University of York, Heslington, York, YO10 5BR, UK; Department of Physics, University of York, Heslington, York, YO10 5BR, UK

Quentin M. Ramasse, SuperSTEM, SciTech Daresbury Campus, Daresbury, WA44AD, UK; School of Chemical and Process Engineering, University of Leeds, Leeds, LS2 9JT, UK; School of Physics, University of Leeds, Leeds, LS2 9JT, UK

Ethan J. Crumlin, Advanced Light Source, Lawrence Berkeley National Laboratory, Berkeley, California 94720, USA

Scott A. Chambers, Physical and Computational Sciences Directorate, Pacific Northwest National Laboratory, 902 Battelle Blvd, Richland WA 99352, USA

Address all correspondence to Kelsey A. Stoerzinger and Scott A. Chambers at kelsey.stoerzinger@pnnl.gov; sa.chambers@pnnl.gov

(Received 22 January 2018; accepted 2 March 2018)

Abstract

Germanium is a small-gap semiconductor that efficiently absorbs visible light, resulting in photoexcited electrons predicted to be sufficiently energetic to reduce H₂O for H₂ gas evolution. In order to protect the surface from corrosion and prevent surface charge recombination in contact with aqueous pH 7 electrolyte, we grew epitaxial SrTiO₃ layers of different thicknesses on *p*-Ge (001) surfaces. Four-nanometer SrTiO₃ allows photogenerated electrons to reach the surface and evolve H₂ gas, while 13 nm SrTiO₃ blocks these electrons. Ambient pressure x-ray photoelectron spectroscopy indicates that the surface readily dissociates H₂O to form OH species, which may impact surface band bending.

Introduction

The direct conversion of solar energy to chemical fuels is a tantalizing route to store renewable energy. By employing photocatalysts to split water into H₂ and O₂ gas,^[1,2] solar energy can be stored in H₂ fuel, subsequently combined with O₂ to produce water and electricity in a cycle free of CO₂ emissions. A “Z-scheme”^[3,4] separates the two constituent reactions—the oxygen evolution reaction (OER) and hydrogen evolution reaction (HER)—so that they occur on separate electrodes, thus decoupling the requirements of band gap and the energy of photoexcited carriers in materials design. Typical oxide photoanodes used to drive the OER have large band gaps,^[5–7] and can thus absorb high-energy photons in a photoelectrochemical (PEC) device, allowing low-energy photons to pass through to the photocathode, which drives the HER.

One semiconductor with attractive light-absorption properties is Ge. In contrast to other semiconductors currently being studied, Ge has a small, indirect band gap of 0.66 eV, as well as a larger optical absorption coefficient across the visible portion of the solar spectrum and into the infrared.^[8] Furthermore, Ge exhibits high room-temperature electron and hole mobilities of 3900 and 1900 cm²/V.s, respectively.^[9] Density functional theory (DFT) calculations indicate that the conduction band (CB) of Ge is higher in energy than hydrogen redox,^[10]

indicating that photoexcited electrons are energetic enough to reduce H₂O to evolve H₂ gas. Thus, the low photovoltage cathode could harness low-energy photons (potentially combining Ge absorbers in series) coupled with a high photovoltage anode to drive solar water splitting. However, interaction with the electrolyte can lead to corrosion of the Ge surface^[11] and recombination of photogenerated electron–hole pairs at surface states,^[12] limiting PEC activity.

We employ controlled passivation^[13] of Ge by epitaxial growth of a wide band-gap semiconductor, SrTiO₃, using oxide molecular beam epitaxy (MBE). By examining a model epitaxial film, we are able to examine charge transport through the heterostructure to yield a critical new understanding of PEC. A similar approach has recently been employed to protect a GaAs photovoltaic.^[14] Growth of SrTiO₃ on Ge has previously been demonstrated for the purpose of investigating associated electrical properties,^[15,16] and we have recently measured the valence band (VB) offset between Ge and SrTiO₃.^[17] These findings support the idea that photoexcited electrons in the Ge would have a downhill path in energy to reach the SrTiO₃ surface.

Here we present the first PEC measurements of the HER on a SrTiO₃ (001)/*p*-Ge (001) heterostructure in neutral (pH 7) electrolyte. This model epitaxial system enables quantification

of the abrupt interface by scanning transmission electron microscopy (STEM), as well as surface stoichiometry and speciation, both post mortem, following electrochemical cycling, and in situ using ambient pressure x-ray photoelectron spectroscopy^[18] (AP-XPS). The Sr/Ti ratio remains similar under all conditions, suggesting that the SrTiO₃ film is stable in the electrochemical environment and supporting its role as a protective cap on Ge, and the surface actively dissociates H₂O to form OH groups. Surface roughness on the Ge substrate leads to pinhole defects, which hinder the efficacy of 4 nm SrTiO₃ film passivation; however, a 13 nm SrTiO₃ film blocks electron transport to the surface. These findings suggest that tailoring SrTiO₃ electronic properties by, for example, doping may provide a promising route for Ge photocathode protection.

Experimental details

Film growth

Ga-doped *p*-Ge (001) substrates (AXT Inc., Fremont, CA, $\rho = 0.04 \Omega\text{-cm}$) were prepared by wet etching procedures described elsewhere.^[19] Following desorption of the chemically prepared oxide at $\sim 600^\circ\text{C}$, the surfaces were clean at the detection limit of x-ray photoelectron spectroscopy (XPS) and exhibited a (2×1) reconstructed surface. Epitaxial growth by oxygen-assisted MBE followed the approach outlined in Jahangir-Moghadam et al.,^[20] as further detailed in ref. [17]. An initial SrGe₂ (001) (3×1) layer was grown at 400°C in vacuum, followed by the growth of 3 unit cells (u.c.) amorphous SrTiO₃ at ambient temperature in 4×10^{-7} Torr O₂, followed by subsequent crystallization at 600°C in vacuum. Additional layers were grown at 300°C in O₂ and annealed at up to 500°C in vacuum to achieve better crystallinity, reaching a final thickness of 5 u.c. (2 nm), 4 nm, or 13 nm SrTiO₃.

Scanning transmission electron microscopy

Cross-sectional STEM samples were prepared using an FEI Helios NanoLab Dual-Beam Focused Ion Beam (FIB)

microscope and a standard lift-out procedure along the Ge [100] and [110] zone axes, with initial cuts made at $30 \text{ kV}/2^\circ$ and final polishing at $1 \text{ kV}/3^\circ$ voltage/incidence angle. High-angle annular dark field (STEM-HAADF) images were collected on a JEOL ARM-200CF microscope operating at 200 kV, with a convergence semiangle of 20.6 mrad and a collection inner semiangle ranging from 68 to 90 mrad. To minimize scan artifacts and improve signal-to-noise, drift-corrected images were prepared using the SmartAlign plugin^[21]; for this, a series of ten frames at 1024×1024 pixels with a fast $2 \mu\text{s px}^{-1}$ dwell time and 90° rotation between frames was used. The frames were upsampled $3 \times$ prior to non-rigid alignment. The inset of Fig. 1(c) was subsequently processed using a lattice-enhanced filter to improve signal-to-noise.^[22]

Electron energy loss spectroscopy (STEM-EELS) maps were collected on a Nion UltraSTEM 100MC “Hermes” microscope operating at 60 kV with a convergence semiangle of 31 mrad and a 44 mrad STEM-EELS collection angle. STEM-EELS maps were collected using 0.37 eV ch^{-1} dispersion, yielding an effective energy resolution of $\sim 1.1 \text{ eV}$. No plural scattering correction was performed, since zero loss measurements confirm that the samples are sufficiently thin ($t/\lambda < 0.5$ inelastic mean free paths). Composition maps are presented in the supplementary information.

Photoelectrochemistry

Films were transferred directly from ultra-high vacuum (UHV) to a N₂-purged glove box for PEC measurements. GaIn eutectic (Sigma, >99.99%) was scratched into the back of the Ge, and a Cu wire held in contact with the pad in a custom-built compression cell. The electrolyte was prepared from Nanopure water ($18.2 \text{ M}\Omega\text{-cm}$) from a mixture of K₂HPO₄ and KH₂PO₄ (Sigma, >99.0%) to achieve a pH of 7 and phosphate concentration of 0.1 M, and bubbled with ultra-high purity N₂ gas before and during data collection. Measurements were made with a CHI-660C potentiostat by cyclic voltammetry at 20 mV/s or

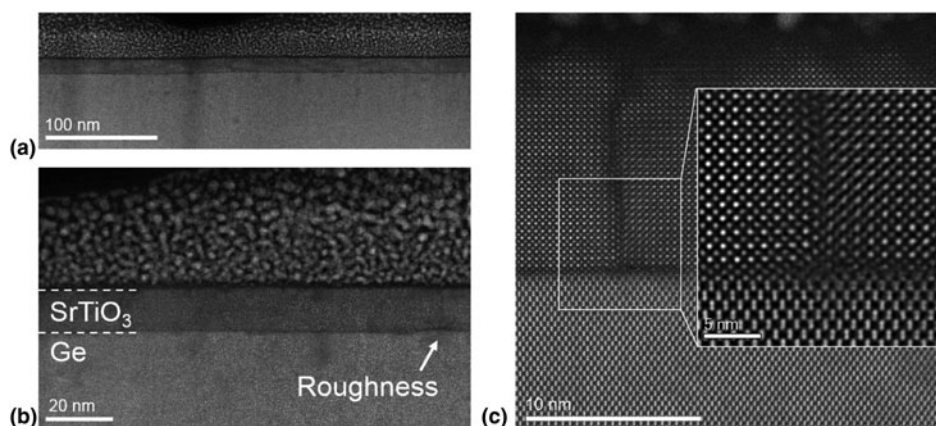


Figure 1. (a) Representative cross-sectional STEM-HAADF image of a 13 nm SrTiO₃/*p*-Ge (001) heterostructure, showing the overall structure along the Ge [110] zone axis. (b) STEM-HAADF image of local Ge substrate roughness. (c) Drift-corrected STEM-HAADF image of a film discontinuity and lattice-filtered inset of an antiphase boundary between two film regions.

constant potential measurements, and voltages corrected for the electrolyte resistance between the working and reference electrodes ($\sim 95 \Omega$ for 4 nm SrTiO₃/Ge). The saturated calomel reference electrode (RE-2BP, ALS Co.) was calibrated to the reversible hydrogen electrode (RHE) scale in the same electrolyte, saturated with H₂ and using Pt working and counter electrodes. A Pt counter electrode (ALS Co.) was also used for PEC measurements.

Light from a 630 nm ultra-high power LED (Prizmatix) was incident through a planar quartz window. The illuminated area of the sample was defined by the PEEK holder, and was commensurate with the area exposed to the electrolyte. The intensity of the LED at the location of the sample was measured after passing through the quartz window with a Newport 843-R power meter, and estimated to attenuate $\sim 10\%$ over the ~ 6 cm path length from water absorption.

X-ray photoelectron spectroscopy

Characterization of the films as-grown and after (photo)electrochemical cycling was performed with an Al K- α source in UHV at room temperature.

AP-XPS was collected at Beamline 9.3.2 at Lawrence Berkeley National Laboratory's (LBNL) Advanced Light Source (ALS).^[23] The 5 u.c. SrTiO₃/Ge was placed directly onto a ceramic heater, held in place by spring-loaded Inconel tips separated with an Al₂O₃ spacer, and grounded through the thermocouple. The thermocouple was pressed into a gold foil placed directly onto the sample surface and isolated from the sample holder clip with an Al₂O₃ spacer.

The incident photon energy (IPE) was calibrated to the Au 4f_{5/2} peak at 84 eV binding energy (BE). The sample was first heated to 300 °C in 100 mTorr O₂ (measured by a calibrated membrane pressure gauge) and characterized. Keeping the sample at 300 °C, the chamber was evacuated to a pressure lower than 1.5×10^{-7} Torr, and 100 mTorr H₂O was introduced into the chamber. The water source was prepared from deionized water (DI; Millipore, >18.2 M Ω ·cm) and degassed by several freeze–pump–thaw cycles. The sample was then cooled in 100 mTorr H₂O.

The O 1s spectra were deconvoluted with Gaussian–Lorentzian peaks using CasaXPS after a Shirley-type background subtraction (Table S1). The O 1s integrated area of the (bi)carbonate peak was calculated from the area of the C 1s (bi)carbonate peak using an O 1s:C 1s relative sensitivity factor, which was experimentally calibrated using the core levels of CO₂ gas.^[24]

Results

Figure 1 shows representative cross-sectional STEM-HAADF images that illustrate the quality of the SrTiO₃ (001)/*p*-Ge (001) film and interface. We observe a relatively uniform film across large areas, as shown in the image of a 13 nm SrTiO₃/Ge interface in Fig. 1(a). We observe no phase separation or impurities, but we do measure some substrate roughness in Fig. 1(b). This roughness is accompanied by film discontinuities and the presence of antiphase boundaries [see inset of

Fig. 1(c)]. We note that the damage at the film surface (top) in this image is the result of long exposure to the electron beam and not characteristic of the film itself.

We found that this structure is highly beam sensitive at 200 kV and that exposure to the electron beam over 30–60 s was sufficient to locally amorphize the structure. To mitigate this problem, we conducted multi-frame, drift-corrected imaging using the SmartAlign plugin^[21,25] to reduce the effective electron dose rate; this approach allowed us to acquire high-resolution images of the film–substrate interface without damaging the underlying structure. Figure 1(c) shows that the interface is extremely abrupt, a finding further supported by STEM-EELS maps of a related 5 u.c. SrTiO₃/Ge heterostructure shown in Fig. S1; these measurements were performed at a lower 60 kV accelerating voltage to avoid excessive sample damage. Taken together, our results illustrate the uniformity, relatively good quality, and sharp interface structure that can be attained through MBE growth of these films.

The band alignment at the SrTiO₃/Ge interface is of critical importance for separation of photogenerated electrons and holes, and the transport of electrons to the surface to reduce H₂O and generate H₂. Previous measurement of the core levels and VB by XPS^[17] indicate that the VB of SrTiO₃ is 3.0 eV lower in energy than that of *p*-Ge. Coupled with the 3.25 eV band gap of SrTiO₃ and the 0.66 eV band gap of Ge, the CB of SrTiO₃ is found to be 0.4 eV below that of Ge. DFT band edge calculations report the Ge CB to be -0.9 V versus normal hydrogen electrode (NHE) at pH 0,^[10] placing the CB of SrTiO₃ in the heterostructure at -0.5 versus NHE (Fig. 2). This is in contrast to the CB of isolated SrTiO₃, reported at -0.26 V versus NHE at pH 0.^[4] Assuming a Nernstian shift of the oxide band edges with increasing pH,^[26] this finding then suggests that the CB of the SrTiO₃/Ge heterostructures

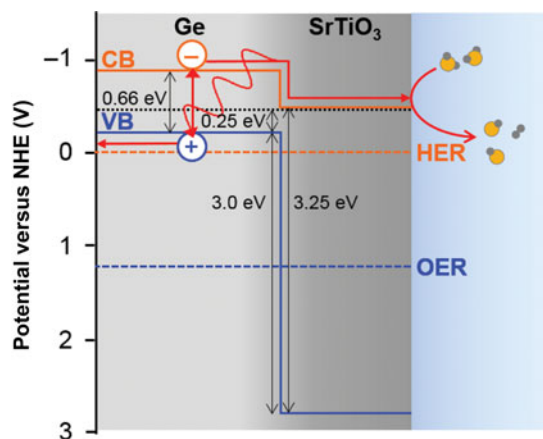


Figure 2. Interface band energy alignment on the NHE scale (pH = 0), obtained from the experimental measurement of VB offset in the heterostructure,^[17] reported CB level of Ge,^[10] and band gap of SrTiO₃. For pH 7 conditions, assuming Nernstian behavior of the oxide band edges would then result in a SrTiO₃ CB at -0.5 V versus RHE.

is at -0.5 V versus RHE in pH 7, resulting in photoexcited electrons being sufficiently energetic to drive the HER.

Following growth, the heterojunctions were transferred directly from UHV to a N_2 -purged glove box for electrochemical characterization in a custom three-electrode cell. The pH 7 phosphate-buffered electrolyte was constantly bubbled with N_2 before and during measurements to minimize buildup of evolved H_2 gas. Figure 3(a) compares the cyclic voltammetry for 4 and 13 nm $SrTiO_3$ on Ge, measured initially in the dark. For the 4 nm film, cathodic current was observed commensurate with the formation of bubbles on the electrode with an onset potential ~ -0.7 V versus RHE in the dark. For the 13 nm film, current was negligible within the tested window. We hypothesize that the 13 nm film acts as a blocking electrode for electrons as seen by the larger resistance measured by high-frequency impedance spectroscopy at open circuit conditions ($>400 \Omega$, compared with $<100 \Omega$ for the 4 nm heterostructure).

Films were then removed from the electrolyte within the purged N_2 box, rinsed with DI water, dried, and returned to UHV for XPS characterization. XPS confirms no electrodeposition of Pt or other contaminants on the film (Figs. S2 and S3). The ratio of Sr 3d to Ti 2p core levels remained similar to that of the as-prepared film [Fig. 3(b)], indicating no preferential leaching of, for example, Sr occurred. This is in contrast

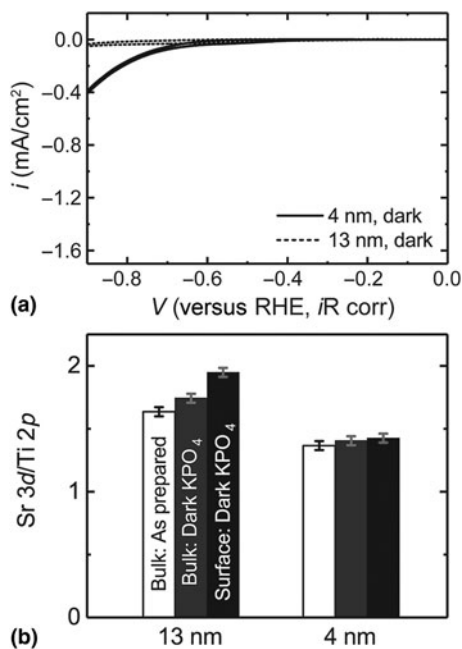


Figure 3. (a) CV curves in dark at 20 mV/s in pH 7, 0.1 M phosphate buffer. The 13 nm $SrTiO_3$ (dashed) acts as a blocking electrode, while the 4 nm film (solid) allows current to be passed to drive HER at high overpotentials. (b) XPS ratio of Sr 3d/Ti 2p core levels measured with $h\nu = 1486$ eV for the as-prepared heterostructure (white) and after cycling in the dark. At 90° incidence (“bulk”), the probe depth is ~ 7 nm, while at 20° incidence (“surface”), it is ~ 2 nm.

to thermodynamic calculations of the Pourbaix diagram at pH 7, which indicate a greater stability of TiO_2 with Sr cations compared with $SrTiO_3$,^[27] and suggests that additional contributors to kinetic stabilization like surface energy and functionalization play an important role. We note, however, that the ratio of the Sr 3d and Ti 2p relative to the Ge 3d for the 4 nm film (where the Ge 3d is observable due to the large probe depth of the >1400 eV kinetic energy photoelectrons) decreased after cycling (Fig. S4), suggesting the roughness of the Ge substrate may expose some pinhole defects in the $SrTiO_3$ film, which grow with cycling.

Upon illumination with an ~ 8 mW 630 nm LED [Fig. 4(a)], the 13 nm $SrTiO_3$ /Ge heterostructure exhibited no change in current density compared with cycling in the dark. In contrast, the 4 nm $SrTiO_3$ /Ge heterostructure exhibited a cathodic photocurrent after initially sweeping below ~ -0.75 V versus RHE. The photocurrent increased with cycle number; however, the dark current remained constant before and after cycling. We hypothesize that this behavior might result from in situ generation of oxygen vacancies in the $SrTiO_3$ film, which would facilitate electron transport to the surface. Chronoamperometry [Fig. 4(b)] illustrates the photocurrent from the 4 nm $SrTiO_3$ /Ge heterostructure directly by switching the LED on and off,

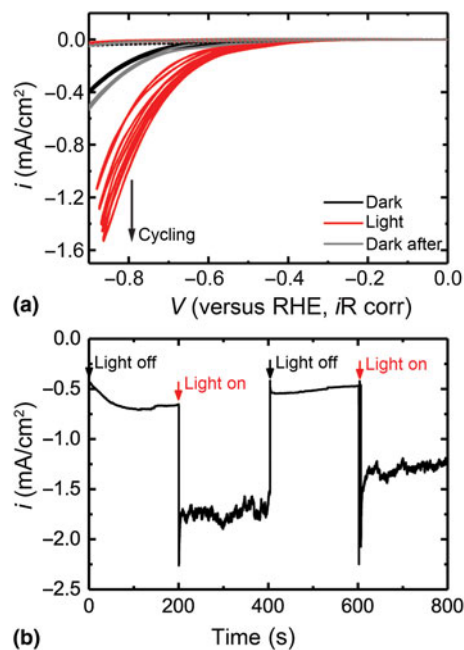


Figure 4. (a) CVs at 20 mV/s in pH 7, 0.1 M phosphate buffer for the 13 nm $SrTiO_3$ (dashed) and 4 nm $SrTiO_3$ (solid) on Ge. Compared with polarization in the dark (black), illumination with a 630 nm LED (red) causes a photocurrent/voltage for the 4 nm film, which increases with cycling. After illumination (gray), the CV is similar to before illumination. (b) Chronoamperometry for 4 nm $SrTiO_3$ /Ge at -0.87 V versus RHE (iR corrected with average current). The dark HER current initially increases, and illumination leads to a constant -1.75 mA/cm² current. Turning the light off returns the current to that previously measured in dark. Repeated illumination gives a similar photocurrent, however this decreases over time.

in contrast to the lack of HER photocurrent from a bare Ge wafer (Fig. S5). The difference between the dark current just before 200 s and the current during illumination after 200 s (where the noise arises from the rapid generation of H₂ bubbles and light scattering) gives a photocurrent of 1.1 mA/cm² at -0.87 V versus RHE. This corresponds to an incident-photon-to-current efficiency (IPCE) of ~14%. We note that the epitaxial nature of the film on the single-crystal Ge substrate results in a roughness factor approaching unity and a highly reflective surface; thus, the photocurrent on a geometric basis and IPCE would be expected to improve greatly by introducing nanostructuring.^[28] Furthermore, the high overpotential is expected to decrease substantially upon incorporation of a co-catalyst.^[29–31] Co-catalysts can improve the onset potential of photocurrent by mechanisms including passivation of surface traps, accumulation of the generated photocarriers, and aiding in charge transfer to reaction intermediates, and will be the subject of a future study.

After >1 h of testing in the dark and illumination, the activity of the 4 nm SrTiO₃/Ge heterostructure decreased with time. Following removal from the cell and copious rinsing to remove salt before introduction to the UHV chamber for XPS, much of the film delaminated, suggesting that pinhole defects in the 4 nm film arising from roughness of the Ge crystal grow with cycling. In contrast, the 13 nm SrTiO₃ film shows comparable ratios of Sr 3*d* and Ti 2*p* and remains sufficiently thick that no Ge 3*d* is observed following cycling under illumination (Fig. S6). Future directions will include cation doping of thicker SrTiO₃ films to ensure *n*-type conductivity persists over the conformal film thickness.

In order to better understand the interface between SrTiO₃ and the electrolyte, we performed AP-XPS in both dry-oxidizing and humid-reducing environments. The tunable IPE at a synchrotron allows the probe depth to be tuned to the top ~1 nm of the film ($h\nu = 690$ eV, O 1*s* core level), and a system of differential pumping and electrostatic lensing enables the surface speciation to be probed in equilibrium with a gas.^[18]

We first consider the surface at 300 °C in 100 mTorr of O₂, similar to growth conditions, which minimizes carbon present from transferring the samples between growth facilities and the synchrotron (Fig. S7). Figure 5 illustrates that the O 1*s* spectra is dominated by bulk-coordinated oxygen of the perovskite crystal,^[24] with some residual CO₃ whose intensity is scaled from that of the CO₃ feature in the C 1*s* inset. When the O₂ is removed from the chamber and H₂O slowly introduced, a feature increases in intensity at ~1.2 eV BE above the bulk (Fig. S8). This feature is attributed to hydroxyl, OH, formation from the dissociation of H₂O on the surface.^[24] In a humid environment, a feature (“Surf”) at higher BE above the bulk is notable, observed from depth profiling (Fig. S9) to be located at the surface. A feature at similar BE offsets located on the surface has been observed for (001)-oriented LaFeO₃ films terminated with the “LaO” plane, but not for the “FeO₂” plane.^[32] We note, however, that on the SrTiO₃ surface, a small phosphorous signal (likely in the form of

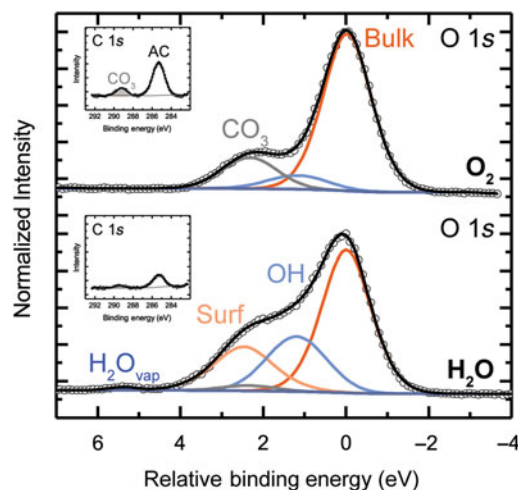


Figure 5. AP-XPS performed at an incident photon energy (IPE) of $h\nu = 690$ eV at 300 °C in 100 mTorr O₂ (top) or 100 mTorr H₂O (bottom). The O 1*s* spectra is shown on a binding energy (BE) scale relative to bulk oxygen (orange), with OH (light blue), CO₃ (gray, intensity determined from the shaded CO₃ feature in the C 1*s* inset), surface oxygen (peach), and H₂O_{vapor} (medium blue) at increasingly higher BE. Some adventitious carbon (AC, C 1*s* inset) remains and attenuates the spectra. Fitting parameters are given in Table S1.

phosphate) was observed in humid environments (Fig. S7), and may also contribute to the signal at this intensity. Adsorption of phosphate species in humid environments may also have implications on the use and role of a PO₄-containing buffer during PEC measurements.^[33]

The notable dissociation of H₂O on the surface of SrTiO₃ to form OH species suggests that during PEC conditions in a neutral electrolyte, SrTiO₃ is likely also hydroxylated. This adsorption of OH species may in turn impact band bending at the surface, of future interest for studies linking surface speciation to the driving force for charge transfer during PEC. In further consideration of the surface stoichiometry in equilibrium with gaseous environments, the ratio of Sr signal to combined Sr and Ti signals remains relatively constant across both dry-oxidizing and humid-reducing conditions, as does the distribution of Sr and Ti with depth (Fig. S10). This further supports ex situ measurements after electrochemically cycling, which indicate that Sr remains stable within the SrTiO₃ film in contact with H₂O at pH 7.

Conclusions

SrTiO₃ was epitaxially grown on *p*-Ge (001) using MBE as a means to protect the surface of the Ge photoabsorber during PEC measurements in aqueous pH 7 electrolyte and maintain an energetically downhill path for photogenerated electrons to reach the solution. The band alignment between SrTiO₃ and Ge is such that the photoexcited electrons can travel through a 4 nm SrTiO₃ capping layer and remain sufficiently energetic to reduce H₂O and evolve H₂ gas in the HER. For 13 nm

SrTiO₃, the film behaves like a blocking electrode, with larger contact resistance and minimal current passed at similar overpotentials compared with the 4 nm film. At -0.87 V versus RHE, the IPCE for 630 nm red light is $\sim 14\%$, noting that the roughness factor of the epitaxial film approaches one and notable reflective losses are not considered in calculation of the IPCE. Thus, the current density would be expected to improve with nanostructuring. Furthermore, the electrode is free of Pt or any other catalyst, and thus its probed intrinsic ability to supply photoexcited electrons to the HER is expected to substantially improve upon deposition of a co-catalyst. Some inherent roughness (on the nm scale) on the Ge surface leads to the presence of pinhole defects in the 4 nm film, resulting in corrosion and film delamination. Future directions include La doping of the SrTiO₃ films to control their carrier concentration such that thicker conformal films can be epitaxially grown and maintain sufficient conductivity for charge transfer.

In situ characterization of the SrTiO₃ (001)/p-Ge (001) heterostructure provides insight into the surface speciation during reaction conditions. AP-XPS was used to characterize the surface under dry-oxidizing and humid-reducing conditions. In contrast to the dry O₂ environment, in a humid environment, SrTiO₃ notably dissociates H₂O to form OH species. This indicates that during the HER in pH 7 aqueous electrolyte, the SrTiO₃ surface likely also contains some hydroxyl species. Future directions will link this speciation to the resultant surface band bending.

Supplementary material

The supplementary material for this article can be found at <https://doi.org/10.1557/mrc.2018.38>

Acknowledgments

AP-XPS and (photo)electrochemistry measurements and analysis were supported for K. A. S. by the Linus Pauling Distinguished Post-doctoral Fellowship at Pacific Northwest National Laboratory (PNNL LDRD 69319). Film growth and characterization was supported at PNNL by the US Department of Energy, Office of Science, Division of Materials Sciences and Engineering under Award No. 10122. The PNNL work was performed in the Environmental Molecular Sciences Laboratory (EMSL), a national science user facility sponsored by the Department of Energy's Office of Biological and Environmental Research and located at Pacific Northwest National Laboratory. PNNL is a multiprogram national laboratory operated for DOE by Battelle. STEM-EELS measurements were carried out at the Super-STEM Laboratory, the UK National Research Facility for Advanced Electron Microscopy, which is supported by the Engineering and Physical Sciences Research Council (EPSRC). This research used resources of the Advanced Light Source, which is a DOE Office of Science User Facility under contract no. DE-AC02-05CH11231.

References

1. T.R. Cook, D.K. Dogutan, S.Y. Reece, Y. Surendranath, T.S. Teets, and D. G. Nocera: Solar energy supply and storage for the legacy and nonlegacy worlds. *Chem. Rev.* **110**, 6474–6502 (2010).
2. M.G. Walter, E.L. Warren, J.R. McKone, S.W. Boettcher, Q. Mi, E. A. Santori, and N.S. Lewis: Solar water splitting cells. *Chem. Rev.* **110**, 6446–6473 (2010).
3. A. Kudo and Y. Miseki: Heterogeneous photocatalyst materials for water splitting. *Chem. Soc. Rev.* **38**, 253–278 (2009).
4. J. Li and N. Wu: Semiconductor-based photocatalysts and photoelectrochemical cells for solar fuel generation: a review. *Catal. Sci. Technol.* **5**, 1360–1384 (2015).
5. B.D. Alexander, P.J. Kulesza, I. Rutkowska, R. Solarska, and J. Augustynski: Metal oxide photoanodes for solar hydrogen production. *J. Mater. Chem.* **18**, 2298–2303 (2008).
6. K. Sivula and R. van de Krol: Semiconducting materials for photoelectrochemical energy conversion. *Nat. Rev. Mater.* **1**, 15010 (2016).
7. W.A. Smith, I.D. Sharp, N.C. Strandwitz, and J. Bisquert: Interfacial band-edge energetics for solar fuels production. *Energy Environ. Sci.* **8**, 2851–2862 (2015).
8. S.M. Sze: *Physics of semiconductor devices* (John Wiley and Sons Hoboken, 1981).
9. M.B. Prince: Drift mobilities in semiconductors. I. Germanium. *Phys. Rev.* **92**, 681–687 (1953).
10. S. Chen and L.-W. Wang: Thermodynamic oxidation and reduction potentials of photocatalytic semiconductors in aqueous solution. *Chem. Mater.* **24**, 3659–3666 (2012).
11. V.R. Erdélyi and M. Green: Hydrogen overpotential on germanium electrodes. *Nature* **182**, 1592 (1958).
12. R. Memming and G. Neumann: Electrochemical reduction and hydrogen evolution on germanium electrodes. *J. Electroanal. Chem. Interfacial Electrochem.* **21**, 295–305 (1969).
13. S. Hu, N.S. Lewis, J.W. Ager, J. Yang, J.R. McKone, and N.C. Strandwitz: Thin-film materials for the protection of semiconducting photoelectrodes in solar-fuel generators. *J. Phys. Chem. C* **119**, 24201–24228 (2015).
14. L. Kornblum, D.P. Fenning, J. Faucher, J. Hwang, A. Boni, M.G. Han, M. D. Morales-Acosta, Y. Zhu, E.I. Altman, M.L. Lee, C.H. Ahn, F.J. Walker, and Y. Shao-Horn: Solar hydrogen production using epitaxial SrTiO₃ on a GaAs photovoltaic. *Energy Environ. Sci.* **10**, 377–382 (2017).
15. M.K. Hudait, M. Clavel, Y. Zhu, P.S. Goley, S. Kundu, D. Maurya, and S. Priya: Integration of SrTiO₃ on crystallographically oriented epitaxial germanium for low-power device applications. *ACS Appl. Mater. Interfaces* **7**, 5471–5479 (2015).
16. M.D. McDaniel, T.Q. Ngo, A. Posadas, C. Hu, S. Lu, D.J. Smith, E.T. Yu, A. Demkov, and J.G. Ekerdt: A chemical route to monolithic integration of crystalline oxides on semiconductors. *Adv. Mater. Interfaces* **1**, 1400081 (2014).
17. S.A. Chambers, Y. Du, R.B. Comes, S.R. Spurgeon, and P.V. Sushko: The effects of core-level broadening in determining band alignment at the epitaxial SrTiO₃(001)/p-Ge(001) heterojunction. *Appl. Phys. Lett.* **110**, 082104 (2017).
18. K.A. Stoerzinger, W.T. Hong, E.J. Crumlin, H. Bluhm, and Y. Shao-Horn: Insights into electrochemical reactions from ambient pressure photoelectron spectroscopy. *Acc. Chem. Res.* **48**, 2976–2983 (2015).
19. P. Ponath, A.B. Posadas, R.C. Hatch, and A.A. Demkov: Preparation of a clean Ge(001) surface using oxygen plasma cleaning. *J. Vac. Sci. Technol. B: Nanotechnol. Microelectron.: Mater. Process. Meas. Phenom.* **31**, 031201 (2013).
20. M. Jahangir-Moghadam, K. Ahmadi-Majlan, X. Shen, T. Droubay, M. Bowden, M. Chrysler, D. Su, S.A. Chambers, and J.H. Ngai: Band-gap engineering at a semiconductor–crystalline oxide interface. *Adv. Mater. Interfaces* **2**, 1400497 (2015).
21. L. Jones, H. Yang, T.J. Pennycook, M.S.J. Marshall, S. Van Aert, N. D. Browning, M.R. Castell, and P.D. Nellist: Smart align—a new tool for robust non-rigid registration of scanning microscope data. *Adv. Struct. Chem. Imaging* **1**, 8 (2015).
22. O.L. Krivanek, M.F. Chisholm, V. Nicolosi, T.J. Pennycook, G.J. Corbin, N. Dellby, M.F. Murfitt, C.S. Own, Z.S. Szilagy, M.P. Oxley, S.

- T. Pantelides, and S.J. Pennycook: Atom-by-atom structural and chemical analysis by annular dark-field electron microscopy. *Nature* **464**, 571 (2010).
23. M.E. Grass, P.G. Karlsson, F. Aksoy, M. Lundqvist, B. Wannberg, B. S. Mun, Z. Hussain, and Z. Liu: New ambient pressure photoemission endstation at advanced light source beamline 9.3.2. *Rev. Sci. Instrum.* **81**, 053106 (2010).
24. K.A. Stoerzinger, W.T. Hong, E.J. Crumlin, H. Bluhm, M.D. Biegalski, and Y. Shao-Horn: Water reactivity on the LaCoO₃ (001) surface: an ambient pressure x-ray photoelectron spectroscopy study. *J. Phys. Chem. C* **118**, 19733–19741 (2014).
25. L. Jones, A. Varambhia, R. Beanland, D. Kepaptsoglou, I. Griffiths, A. Ishizuka, F. Azough, R. Freer, K. Ishizuka, D. Cherns, Q.M. Ramasse, S. Lozano-Perez, and P.D. Nellist: Managing dose-, damage- and data-rates in multi-frame spectrum-imaging. *Microscopy* (In press), DOI: 10.1093/jmicro/dfx125 (2018).
26. Y. Ping, R. Sundararaman, and W.A. Goddard III: Solvation effects on the band edge positions of photocatalysts from first principles. *Phys. Chem. Chem. Phys.* **17**, 30499–30509 (2015).
27. I.E. Castelli, K.S. Thygesen, and K.W. Jacobsen: Calculated Pourbaix diagrams of cubic perovskites for water splitting: stability against corrosion. *Top. Catal.* **57**, 265–272 (2014).
28. L.N. Quan, Y.H. Jang, K.A. Stoerzinger, K.J. May, Y.J. Jang, S. T. Kochuveedu, Y. Shao-Horn, and D.H. Kim: Soft-template-carbonization route to highly textured mesoporous carbon-tio₂ inverse opals for efficient photocatalytic and photoelectrochemical applications. *Phys. Chem. Chem. Phys.* **16**, 9023–9030 (2014).
29. K.C. Kwon, S. Choi, K. Hong, D.M. Andoshe, J.M. Suh, C. Kim, K.S. Choi, J.H. Oh, S.Y. Kim, and H.W. Jang: Tungsten disulfide thin film/p-type Si heterojunction photocathode for efficient photochemical hydrogen production. *MRS Commun.* **7**, 272–279 (2017).
30. J.E. Thorne, Y. Zhao, D. He, S. Fan, S. Vanka, Z. Mi, and D. Wang: Understanding the role of co-catalysts on silicon photocathodes using intensity modulated photocurrent spectroscopy. *Phys. Chem. Chem. Phys.* **19**, 29653–29659 (2017).
31. D.V. Esposito, I. Levin, T.P. Moffat, and A.A. Talin: H₂ evolution at Si-based metal–insulator–semiconductor photoelectrodes enhanced by inversion channel charge collection and H spillover. *Nat. Mater.* **12**, 562 (2013).
32. K.A. Stoerzinger, R. Comes, S.R. Spurgeon, S. Thevuthasan, K. Ihm, E. J. Crumlin, and S.A. Chambers: Influence of LaFeO₃ surface termination on water reactivity. *J. Phys. Chem. Lett.* **8**, 1038–1043 (2017).
33. M. Favaro, F.F. Abdi, M. Lamers, E.J. Crumlin, Z. Liu, R. van de Krol, and D.E. Starr: Light-induced surface reactions at the bismuth vanadate/potassium phosphate interface. *J. Phys. Chem. B* **122**, 801–809 (2018).